ACS OMEGA

Open Access

http://pubs.acs.org/journal/acsodf

Article

Growth Kinetics and Porous Structure of Surfactant-Promoted Gas Hydrate

Belkacem Samar,* Saphir Venet, Arnaud Desmedt, and Daniel Broseta*

Cite This: *ACS Omega* 2024, 9, 31842−31854

Read Online

ACCESS | Metrics & More | Article Recommendations | Supporting Information

ABSTRACT: Surfactants present in tiny amounts in the aqueous phase are known to be efficient gas hydrate promoters; yet, the promotion mechanisms are still not fully understood. Understanding and directing those mechanisms is key to the implementation of gas-hydrate-based applications such as gas storage and separation, secondary refrigeration or water treatment, and desalination. In this work, the growth at the water/gas interface and the porous structure of surfactant-promoted methane hydrate are observed by optical microscopy and Raman imaging in glass capillaries used as optical cells. Hollow crystals are continuously generated and expelled from the methane/water meniscus into the water or surfactant solution, where they ultimately form the skeleton of a porous medium filled with the solution. Unprecedented information is gathered over a range of scales from the molecular scale (crystal structure and cage filling) to the mesoscale (crystal morphologies, growth habits and pore sizes) and macroscale (rates and amounts of water and gas converted into hydrate and hydrate porosity). Following an early steady-state growth regime, a sudden order-of-magnitude increase of the conversion rate occurs, which is related to gaseous methane microbubbles being directly incorporated across the meniscus in the aqueous solution and later converted to methane hydrate. An assessment and comparison are made of the mechanisms and performance of two common anionic surfactants known to be efficient gas hydrate promoters, SDS (sodium dodecyl sulfate) and AOT (dioctylsulfosuccinate sodium or AerosolOcTyl). AOT provides a quicker but more limited conversion into hydrate than SDS, suggesting that it is more appropriate for continuous flow processes while SDS is better suited for gas storage applications. Raman spectra reveal that cage filling by methane of structure I methane hydrate is not affected by surfactants.

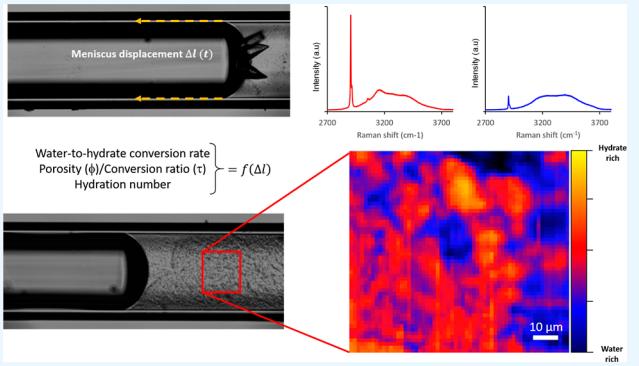

1. INTRODUCTION

Gas hydrates are solid, nonstoichiometric inclusion compounds in which guest molecules (or hydrate formers) are trapped into polyhedral cavities made up of water (host) molecules.[1,2] Under appropriate temperature and pressure conditions, these compounds nucleate and grow predominantly where both the host and guest phases are present, that is, at water/guest interfaces. Once nucleation occurs, these interfaces quickly cover up with a low-permeable thin polycrystalline hydrate layer (or crust), which hinders further conversion into hydrate of the water and guest molecules left on either side of the interfaces. Methods that consist of generating fine dispersions of the two phases are efficient because of the large water/guest interfacial area available for hydrate formation and growth, but it usually requires a lot of mechanical energy.[3] Under quiescent conditions, one route for overcoming this mass-transfer limitation relies on the use of anionic surfactants added in tiny amounts (a few hundreds of ppmw) to the aqueous phase, which act to promote gas hydrate formation through mechanisms that are still poorly understood.[4−6] A better characterization and understanding of those mechanisms is key for increasing the TRL (technology readiness level) of gas-hydrate-based technologies,[7] such as natural gas storage[8,9] and separation,[10−13] water treatment or desalination,[14,15] and secondary refrigeration.[16−18] Gas separation and water treatment or desalination involve a continuous flow that requires high gas hydrate throughputs, i.e., high conversion rates, whereas gas storage or secondary refrigeration requires high conversion levels; in the latter application, enough liquid water should be left unconverted to ensure flowability (see Figure 1).

This paper presents an experimental methodology combining optical microscopy and in situ microRaman spectroscopy to provide insights into the mechanisms of surfactant-promoted gas hydrate formation and growth, as well as the structure and properties of the resulting hydrate. Those

Received: April 4, 2024
Revised: May 29, 2024
Accepted: May 31, 2024
Published: July 12, 2024

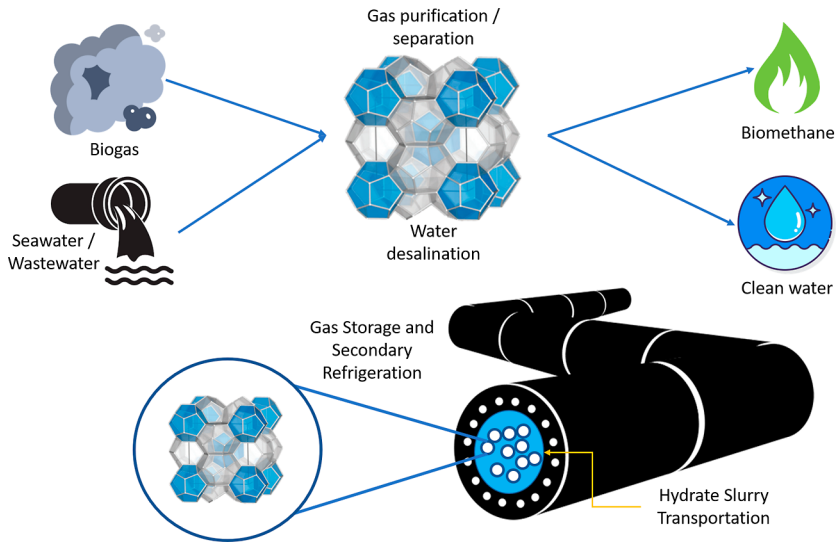

Figure 1. Potential gas-hydrate-based applications involving methane, CO_2, or a mixture of these two compounds, shown in increasing order of TRL: biogas purification, water desalination and treatment, natural gas storage and secondary refrigeration.

mechanisms and structure are not fully understood yet, and their understanding and control would benefit the potential applications cited above. This methodology, which provides information over a large range of molecular to macroscopic scales, is implemented with two prototypical surfactant promoters, SDS (sodium dodecyl sulfate) and AOT (dioctyl sulfosuccinate sodium salt or AerosolOcTyl). SDS is a benchmark promoter, to which other surfactant promoters are usually compared;[4,19,20] it is often used in combination with other additives, including thermodynamic promoters,[21,22] solid porous or nonporous particles,[23−29] or soil organic matter.[30]

The phenomenon of gas hydrate promotion by surfactants has been investigated for more than three decades. The first experimental evidence stemmed from the large and rapid pressure or temperature variations observed in large-volume cells containing initially the aqueous surfactant solution and gas (most often methane) and driven into hydrate formation conditions.[19,31−36] These variations witness the conversion of water and gas molecules into gas hydrate. In cells equipped with see-through windows, a porous hydrate is observed to form and climb over the windows and cell walls and pump the aqueous phase,[35,37] a process referred to as the wall-climbing or capillary effect. This phenomenon does not seem to be connected with the occurrence of a critical micellar concentration in the aqueous solution,[4,38−42] as hypothesized in early studies.[33,43] Further tentative explanations of the promoting effect involve surfactant adsorption onto hydrate crystals,[44−46] an increased hydrate interfacial area and a decreased adhesion between hydrate particles. Enhanced presence of the hydrate former in the bulk aqueous solution has been observed concomitant to SDS-promoted hydrate growth.[47] As pointed out above, some substrates favor the growth of porous hydrates,[48−50] even though the hydrate crystals are generated at aqueous solution/gas interfaces,[51−55] in a manner not yet fully understood.

The purpose of this paper is to shed light into the mechanisms that govern gas hydrate promotion by surfactants. It reports small-scale (i.e., micro- and mesoscale) observations of the generation and growth process and the structure of the resulting porous hydrate, as well as the macroscopic features that characterize hydrate growth and the efficiency of a given promoter, such as the rate and amount of hydrate conversion. Hydrate generation is observed by optical microscopy near/around the interface (meniscus) separating the aqueous surfactant solution and the methane phase in a thin glass capillary acting as an optical cell. The position and displacement of that meniscus are directly related to the volumes and proportions of the various phases (hydrate, aqueous, and gas phases) present in the capillary and their variation over time. The combination of those observations with microRaman imaging provides information on the hydrate growth features and final structure of the hydrate mass formed over a very large range of spatial scales: at microscopic (or molecular) scales, the structure and cage filling of the hydrate crystal; at mesoscopic scales, the hydrate generation process on the water/guest meniscus and the structure (pore size) of the porous hydrate; and at macroscopic scales, the rate and amount of conversion of the water and guest into hydrate. This methodology is implemented for the two surfactants cited above, whose hydrate-promoting properties can thus be precisely evaluated and compared.

2. EXPERIMENTAL SETUP AND PROCEDURES—OUTLINE OF THE STUDY

The experimental setup and procedures are very similar to those recently used for examining various gas hydrate properties in our[55−57] and other[50,58−64] laboratories. The optical cell is a round glass capillary with its internal radius r well below the millimeter (r = 100 μm in this study), filled with a column of a few millimeters of aqueous solution and then flame-sealed at one end. The aqueous solution is displaced to this end by centrifugation. The other open end of the capillary is glued to a stainless-steel tube with an outer diameter of 1/16″, which is connected to a high-pressure pump containing the gas (methane) used in the pressure-controlled mode. The air initially present in the capillary is eliminated through repeated compression and purges. The aqueous solutions considered in this work consist of deionized water with a small amount (500 ppmw) of an anionic surfactant, either SDS (sodium dodecyl sulfate) or AOT (dioctyl sulfosuccinate

https://doi.org/10.1021/acsomega.4c03251
ACS Omega 2024, 9, 31842−31854

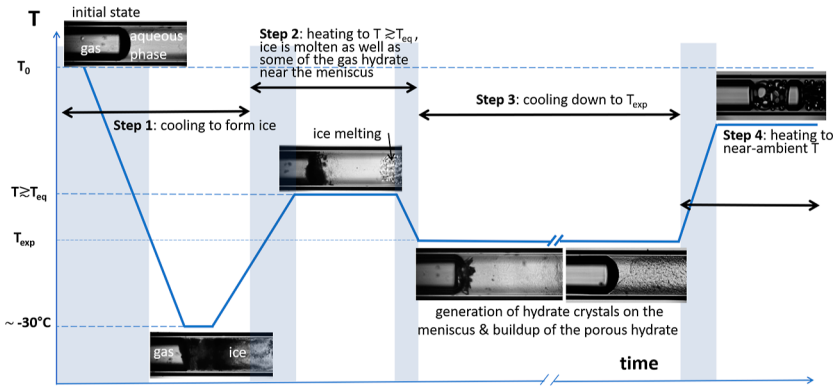

Figure 2. Temperature sequence in a typical experiment of hydrate formation (steps 1 and 2), growth at T_{exp} and P_{exp} (step 3), and dissociation (step 4) at near-ambient temperature $T_0 > T_{eq}$, the equilibrium temperature of methane hydrate at P_{exp}. The snapshots are extracted from the video TCYCLE in the Supporting Information. The abscissa is not to scale; the duration of step 3 is much larger than that of other steps (see text).

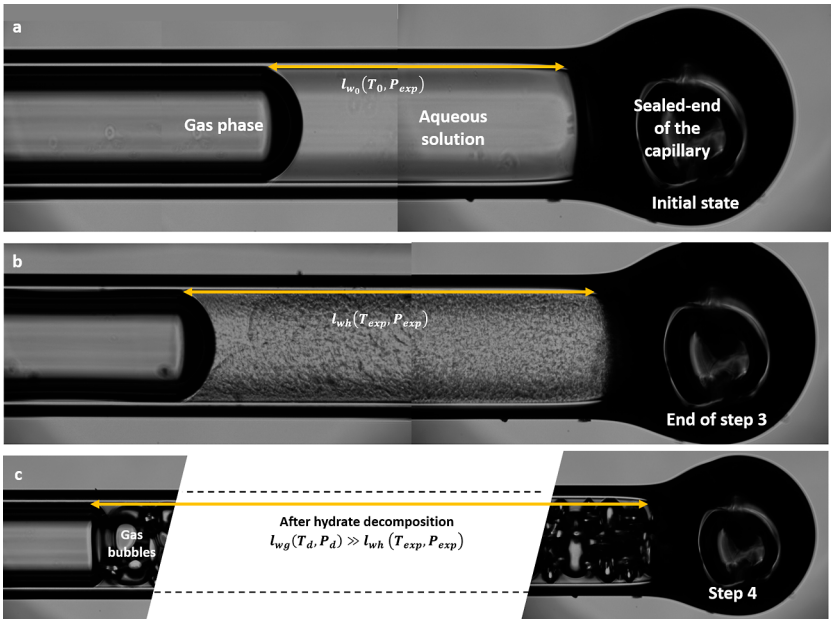

Figure 3. Reconstructed images of the glass capillary at various steps (see Figure 1) of hydrate formation, growth, and dissociation processes (obtained from the video MATBAL in the Supporting Information). P_d and T_d in image (c) denote the chosen pressure and temperature of hydrate dissociation to measure l_{wg}.

sodium salt, known under its commercial name: AerosolOc-Tyl), both being excellent methane hydrate promoters.[46,53]

The capillary, loaded with the two aqueous and gas phases separated by a meniscus at the pressure of the experiment, is placed in a heating−cooling stage (Linkam CAP500) that allows control of its position in the two horizontal directions (over a distance of ± 2.5 cm along the axis of the capillary), under the objective of a microscope used either in the transmission mode with video-monitoring (particularly in the meniscus region) or with confocal microRaman spectroscopy to provide the Raman spectral signatures of selected cross-sections within the sample. With a 532 nm incident wavelength, a grating of 600 grooves/mm, and a 50× long-distance objective, the spatial resolution is close to the micrometer in the horizontal directions, and the spectral resolution in the range of 3 cm^{-1}. The spectral region probed is the interval 2700−3800 cm^{-1}, in which the presence of two narrow bands at 2903 and 2914 cm^{-1} witnesses the stretching modes of the methane confined, respectively, in the large and small cages of the sI hydrate, whereas the broad bands between 3000 and 3600 cm^{-1} are the signatures of liquid water.[2,65−69] (For more details, see the pdf file in the Supporting Information.)

In all experiments, pressure is kept constant during the hydrate growth process; here, P_{exp} = 40 bar. Temperature is the control parameter, which is driven back and forth first across the ice melting temperature to generate and melt the ice (steps 1 and 2 in Figure 2) and then across the methane hydrate equilibrium temperature (here, T_{eq} = 4.2 °C at P_{exp} = 40 bar) to grow (step 3) and then dissociate (step 4) the hydrate. Step 3 is where the growth of the hydrate is monitored at a fixed experimental temperature T_{exp} ($<T_{eq}$) or fixed distance to the equilibrium temperature (or driving force) $\Delta T = T_{eq} - T_{exp}$, referred to as the subcooling. The hydrate growth experiments reported and discussed below have been conducted under low/moderate subcooling, $\Delta T \approx 2$ and 4 °C.

Starting with the aqueous and gas (methane) phases at P_{exp} and near-ambient T separated by an interface (meniscus) (cf. Figure 3a), the gas hydrate is not formed directly by driving the system from room temperature to the targeted

https://doi.org/10.1021/acsomega.4c03251
ACS Omega 2024, 9, 31842−31854

experimental temperature T_{exp}, as this would require a considerable amount of time to nucleate the hydrate. It is formed through ice formation and melting: first, ice is formed by dropping T from the ambient temperature to ≈−30 °C (step 1 in Figure 2) and then (step 2) melted together with the gas hydrate formed (if any) by raising T to slightly above the hydrate equilibrium temperature T_{eq} and finally by decreasing T to the targeted temperature T_{exp}. The duration of both steps 1 and 2 is short (only for a few tens of seconds). T is then kept constant at that value T_{exp} over step 3 of the experiment, where hydrate crystals are continuously generated on the gas/water meniscus and expelled on the water side of the meniscus. This process (step 3), which lasts a few hours (dependent on subcooling and obviously on the initial amount of water), ends when the slurry of hydrate crystals consolidates into a porous medium (see Figure 3b and video TCYCLE in the Supporting Information).

Section 4.1 reports three hydrate growth experiments: in two experiments, the surfactant promoter is either SDS or AOT and the subcooling is $\Delta T \approx 2$ °C ($T_{exp} \approx 2.3$ °C), and in the third experiment the surfactant is SDS and the subcooling is $\Delta T \approx 4$ °C ($T_{exp} \approx 0.3$ °C), similar to the conditions recently considered by Venet et al.[55] The surfactant concentration of 500 ppmw is the same in all three experiments. Venet et al.[55] used in situ microRaman spectroscopy to image the resulting porous medium, made up of a hydrate skeleton filled with the aqueous solution, but did not focus on the hydrate growth process. In the work reported in this article, the hydrate growth process is carefully monitored by observing the meniscus region, together with the porosity of the resulting porous hydrate or, equivalently, the amount of water or gas converted into hydrate. The latter quantities are determined by melting (or dissociating) the hydrate at $T_d > T_{eq}$ (step 4 of the experiment) and inferring from the position of the meniscus the volume of released gas, which forms a stable gas-in-water emulsion.

The main novelty of the proposed methodology, which is presented in detail in the next Section and illustrated with three examples in Section 4.1, is the exploitation of the meniscus motion and positions during the hydrate formation and growth process (step 3) and the following dissociation step (step 4). This exploitation is combined with the observation of the crystallization process taking place on/near the meniscus (see Section 4.1) and thus provides both qualitative and quantitative information as to both the hydrate formation kinetics and the phenomena responsible for these kinetics, that is, the generation of hydrate crystals on the water/gas interface. The characterization of the resulting porous hydrate by in situ Raman spectroscopy imaging is reported in Section 4.2.

3. EXPLOITATION OF THE MENISCUS POSITIONS AND DISPLACEMENTS

The meniscus positions and displacements measured as the gas hydrate is generated and then melted provide information as to the rate and amount of water (or gas) converted into hydrate and the porosity of the resulting hydrate—defined as the fraction of hydrate mass not occupied by the hydrate skeleton and filled with the aqueous phase.

Water molecules occupy a larger volume in the hydrate than in the aqueous phase, which induces an increase in the volume of the aqueous phase, where the hydrate crystals accumulate and grow: the motion of the meniscus between this phase and the bulk guest phase (methane) is related to the amount of water converted into hydrate, which is proportional to the gas uptake or the quantity of gas enclathrated in the hydrate—the number of moles of water converted is N_h times the number of moles of gas enclathrated, where N_h (≈6 for methane hydrates) is the hydration number, i.e, the number of water molecules per guest (i.e., methane) molecule enclathrated in the hydrate. At the end of the experiment, when the hydrate has been dissociated, the meniscus moves further as the liberated gas forms an emulsion and occupies an additional volume within the aqueous phase. This section can be read in parallel to the next section, which reports three experiments conducted with SDS or AOT as hydrate promoters.

Figure 3 shows snapshots of the system at various steps of the experiment, where l (with appropriate subscript) denotes the column length, i.e., the length between the meniscus and the sealed end of the capillary. Owing to the large aspect ratio of the cylindrical column, this length is precisely related to the total volume of the phase(s) that is (are) located between the meniscus and the capillary closed end: the volume of the aqueous phase $\pi r^2 l_{w_0}$ at the start of the experiment (step 1), the volume $\pi r^2 l(t)$ of the aqueous phase plus the hydrate phase while the latter is growing with time t (step 3), and the volume $\pi r^2 l_{wg}$ of the aqueous phase plus the gas released from the hydrate when melted at the end of the experiment (step 4).

As the interest is in volume variations, the column length l can be measured by considering either the base or the pole of the meniscus, provided that indeed the contact angle does not vary during the experiment. The base of the meniscus, i.e., the position of the water/gas/glass triple line, is considered in this work for reasons that are presented and discussed in the pdf file in the Supporting Information.

At the start of the experiment, the length l_{w_0} of the water column is measured at the pressure of the experiment P_{exp} and a temperature near room temperature, usually $T_0 \approx 10$ °C. The corresponding volume $\pi r^2 l_{w_0}$ contains a number of moles of water

$$n_{w_0} = \frac{\pi r^2 l_{w_0}}{\nu_{wl}}. \quad (1)$$

where $\nu_{wl} \approx 18$ cm^3 is the volume of 1 mole of liquid water. This volume can be assumed to be constant in the pressure and temperature intervals of interest in this work (see the pdf file in the Supporting Information).

Following steps 1 and 2 (ice formation and ice melting), the column length l increases in the course of gas hydrate formation (step 3, where $T = T_{exp}$ and $P = P_{exp}$ are kept constant) as a result of liquid water being converted into hydrate crystals: 1 mole of water incorporated in the hydrate lattice occupies a volume $\nu_{wh} \approx 22.6$ cm^3 (Sloan and Koh[1] and Handa[70]) rather than 18.0 cm^3 in the aqueous phase, a ≈ 25% increase. ν_{wh} is assumed to be constant in the pressure and temperature intervals of interest here.

A meniscus displacement dl is thus related to the number of moles of water enclathrated into the hydrate dn_h as follows

$$\pi r^2 dl = (\nu_{wh} - \nu_{wl}) dn_h \quad (2)$$

where dn_h is also equal to dn_g, which is the number of moles of gas (methane) enclathrated in the hydrate phase, times the hydration number N_h (≈6 for methane hydrate)

https://doi.org/10.1021/acsomega.4c03251
ACS Omega 2024, 9, 31842−31854

$$dn_h = N_h \times dn_g \quad (3)$$

The overall meniscus displacement at time t, $\Delta l(t) = l(t) - l_{w_0}$, where $l_{w_0} = l_w(t = 0)$ is the initial position of the meniscus, is related to the water conversion ratio $\tau_w(t) = n_h(t)/n_{w_0}$, or the fraction of water molecules initially present in the capillary that have been incorporated into the hydrate phase at time t as follows

$$\tau_w(t) = \frac{n_h(t)}{n_{w_0}} = \frac{\nu_{wl}}{\nu_{wh} - \nu_{wl}} \frac{\Delta l(t)}{l_{w_0}} \quad (4)$$

The water conversion rate $d\tau_w/dt$ $_w$ $d\tau/dt$ is thus proportional to the meniscus velocity dl/dt

$$\frac{d\tau_w}{dt} = \frac{\nu_{wl}}{\nu_{wh} - \nu_{wl}} \frac{d(\Delta l/l_{w_0})}{dt} \quad (5)$$

τ_w is proportional to the more familiar gas uptake normalized by the quantity (number of moles) of water initially present, $\tau_g = \tau_w/N_h$.[29,30] τ_w does not exceed 1, and the maximum normalized gas uptake is therefore $1/N_h$.

Equations 4 and 5 have been obtained by equating the total volume of hydrate phase and of unconverted liquid water, i.e., $\pi r^2 l(t)$, to the sum of the hydrate volume equal to $n_h \nu_{wh} = \tau n_{w_0} \nu_{wh}$ and the remaining (unconverted) water equal to $(n_{w_0} - n_h)\nu_{wl} = (1 - \tau) n_{w_0} \nu_{wl}$

$$\pi r^2 l(t) = \tau_w(t) \frac{\pi r^2 l_{w_0}}{\nu_{wl}} \nu_{wh} + [1 - \tau_w(t)] \frac{\pi r^2 l_{w_0}}{\nu_{wl}} \nu_{wl} \quad (6)$$

In the late stages of step 3, the conversion process slows down, and the column length l reaches a stable value, denoted l_{wh}, corresponding to the arrest of the meniscus. The final conversion ratio is related to the meniscus displacement $\Delta l_{wh} = l_{wh} - l_{w_0}$ during the whole duration of step 3 as follows

$$\tau_{wf} = \frac{\nu_{wl}}{\nu_{wh} - \nu_{wl}} \frac{\Delta l_{wh}}{l_{w_0}} \quad (7)$$

In the very late stages of step 3, some hydrate is sometimes observed to creep on the capillary walls on the gas side of the meniscus, which renders the determination of the final length l_{wh} difficult: in these cases, the final length l_{wh} is measured prior to the occurrence of those deformations.

At the end of step 3, when the hydrate-rich medium no longer evolves with elapsed time (see Venet et al.[55]), the texture appears to be homogeneous over the interval between the meniscus and the closed end of the capillary, which justifies a description in terms of a porous medium with porosity ϕ—the ratio of the pore volume (i.e., the volume filled with the unconverted aqueous phase) to the total volume (i.e., the volume of the hydrate skeleton plus the pore volume)

$$\phi = \frac{(1 - \tau_{wf})\pi r^2 l_{w_0}}{\pi r^2 l_{wh}} = \frac{(\nu_{wl} l_{wh} - \nu_h l_{w_0})}{(\nu_{wl} - \nu_{wh}) l_{wh}} \quad (8)$$

ϕ is closely related to the final water conversion ratio τ_{wf}

$$\phi = \frac{\nu_{wl}(1 - \tau_{wf})}{(\nu_{wh} - \nu_{wl})\tau_{wf} + \nu_{wl}} \quad (9)$$

If the medium is not homogeneous, then ϕ as defined above is the average porosity of the medium over the interval between the meniscus and the closed end of the capillary.

Porosities vary from 1 (no water conversion into hydrate: $\tau_{wf} = 0$) to 0 (full water conversion: $\tau_{wf} = 1$), corresponding to a meniscus that, over the time scale of the experiment, respectively, does not move ($l_{wh} = l_{w_0}$) and moves to the maximum extent $l_{wh} = \nu_{wh} l_{w_0}/\nu_{wl} \approx 1.26 l_{w_0}$. τ_{wf} and $(1 - \phi)$, or ϕ and $(1 - \tau_{wf})$, can be considered as proxies of each other: ϕ is lower than $(1 - \tau_{wf})$ by less than 5% over the entire interval from 0 to 1.

For typical porosities ϕ in the 40−70% range (or conversion ratios τ_{wf} in the 30−60% range), the overall meniscus displacement Δl_{wh} is in the order of 5−10% of the initial length l_{w_0} (see the examples in the next section): a large initial amount of aqueous solution (i.e., a large l_{w_0}) is therefore recommended for a more accurate determination of Δl_{wh}.

A more precise determination of ϕ or τ_{wf} is obtained by melting the hydrate, e.g., by raising T to above T_{eq}, say, to $T_d \approx$ 10−20 °C (step 4 in Figure 2): the released gas forms bubbles in the aqueous solution, whose volume adds up to that of the aqueous phase. The total column length l_{wg} of the aqueous solution + gas bubbles (Figure 3c) is therefore equal (up to a factor πr^2) to the initial water volume, l_{w_0} (measured at the beginning of the experiment), plus the volume of the gas released at T_d ($>T_{eq}$) and P_d(step 4). The difference between those two lengths, $\Delta l_{wg} = l_{wg} - l_{w_0}$, thus provides n_g the number of moles of gas enclathrated in the hydrate phase during step 3, i.e., at T_{exp} and P_{exp}

$$n_g = \frac{\pi r^2 \Delta l_{wg}}{\nu_g} \quad (10)$$

where ν_g the molar volume of the guest (here, methane) at T_d and P_d is obtained using the NIST database.[71] The number of moles of water n_h converted into hydrate is n_g times the hydration number N_h, hence

$$n_h = n_g N_h = N_h \frac{\pi r^2 \Delta l_{wg}}{\nu_g} \quad (11)$$

Another expression is thus obtained for the total (or final) conversion ratio

$$\tau_{wf} = \frac{n_h}{n_{w_0}} = N_h \frac{\Delta l_{wg}}{l_{w_0}} \frac{\nu_{wl}}{\nu_g} \quad (12)$$

that can be equated to eq 7 to obtain the hydration number N_h

$$N_h = \frac{\Delta l_{wh}}{\Delta l_{wg}} \frac{\nu_g}{\nu_{wh} - \nu_{wl}} \quad (13)$$

The n_h moles of water enclathrated in the hydrate phase occupy a (hydrate) volume

$$V_h = n_h \nu_h = N_h \frac{\pi r^2 \Delta l_{wg} \nu_{wh}}{\nu_g} \quad (14)$$

The pore space is occupied by the $n_{w_0} - n_h$ moles of unconverted water and therefore has a volume V_p

$$V_p = (n_{w_0} - n_h)\nu_{wl} = \left(\frac{\pi r^2 l_{w_0}}{\nu_{wl}} - N_h \frac{\pi r^2 \Delta l_{wg}}{\nu_g} \right) \nu_{wl} \quad (15)$$

https://doi.org/10.1021/acsomega.4c03251
ACS Omega 2024, 9, 31842−31854

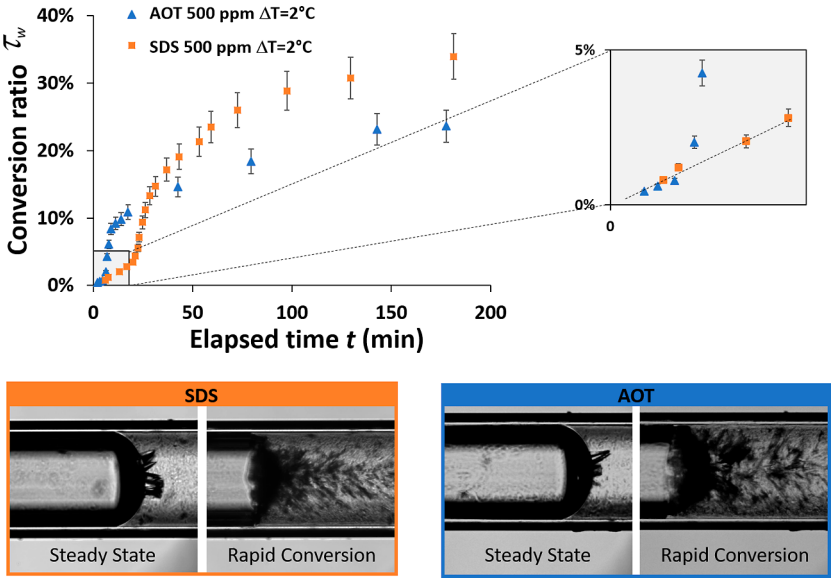

Figure 4. Conversion ratio or meniscus displacement—both quantities are proportional, see eq 4—as a function of time t for the two surfactants investigated. Bottom: snapshots of the meniscus region in the early steady-state and rapid conversion regimes.

The porosity $\phi = V_p/(V_p + V_h)$ of the porous medium made of the hydrate skeleton filled with the aqueous phase is therefore

$$\phi = \frac{1 - \frac{\nu_{wl}}{\nu_g} N_h \left(\frac{\Delta l_{wg}}{l_{w_0}}\right)}{1 + N_h \left(\frac{\Delta l_{wg}}{l_{w_0}}\right)\left(\frac{\nu_{wh} - \nu_{wl}}{\nu_g}\right)} \tag{16}$$

As expected, the absence of water conversion into hydrate ($\tau_{wf} = 0$, $\phi = 1$) corresponds to a meniscus that has not moved in the course of the experiment: $l_{wg} = l_{w_0}$. On the other hand, full water conversion ($\tau_{wf} = 1$, $\phi = 0$) corresponds to a maximum displacement of the meniscus $\Delta l_{wg} = l_{w_0}\nu_g/(N_h\nu_{wl})$, or $\Delta l_{wg} \approx 6 l_{w_0}$ for $P_d = P_{exp} = 40$ bar and the temperatures of interest. For typical porosities in the range of 50−70%, Δl_{wg} lies in the range of 2−4 times the initial length l_{w_0} for those pressure and temperatures, which means that the meniscus is displaced far (a few cms away) from its initial position. If the meniscus is not accessible with the objective of the microscope, P is increased to $P_d > P_{exp}$ in the end (step 4) of the experiment to reduce Δl_{wg}: ν_g in the above equation is then the gas molar volume at T_d and P_d.

To the best of our knowledge, very few attempts have been made to quantitatively exploit the meniscus position to monitor gas hydrate growth and to measure the gas uptake by melting the final hydrate-rich domain. Ou et al.[59] monitored the growth under strong subcooling of a single CO_2 hydrate crystal placed in liquid water at some distance from a water/guest interface. This crystal grew only toward that interface, witnessing the diffusive transport of CO_2 through water. Both the distance and the size of the crystal were measured as a function of time, from which the authors inferred both the hydration number of the CO_2 hydrate and the hydrate growth kinetic parameters. In another recent investigation, Sun et al.[64] observed the growth under moderate subcooling of a single CH_4 hydrate crystal placed not far from a gas (CH_4) bubble surrounded by liquid water. The shrinkage of this bubble, i.e., gas consumption, provided a precise determination of the hydrate growth kinetics.

A popular metric makes use of gas storage capacity, defined as the volume of gas (under standard temperature and pressure conditions) relative to the hydrate volume, which lies in the range of 160−170 for methane hydrates with low porosity or liquid water content. This capacity is related in a simple manner to the quantities defined and used in this study, τ_{wf} and ϕ (see the pdf file in the Supporting Information).

4. RESULTS

4.1. Surfactant-Promoted Growth: Buildup of the Porous Hydrate. This section parallels the previous section: it reports and exploits the meniscus displacements $\Delta l(t)$ of two gas hydrate-forming systems, methane at $P = 40$ bar and an aqueous solution containing 500 ppmw of either SDS or AOT, together with video- and micrographs of the meniscus region, where hydrate crystals are continuously generated and expelled on the water side. Both features are monitored at the same time: the crystallization processes at/around the meniscus and the motion of that interface that results from these processes. Finally, the porosity of the resulting porous hydrate is determined by using the procedure described in the previous section, i.e., by measuring the quantity of gas released upon melting the porous hydrate. The purpose is 2-fold: (i) to illustrate the proposed experimental methodology with examples and (ii) to identify the hydrate-promoting mechanisms of those two surfactants and compare their efficiencies for the particular conditions (of subcooling and surfactant concentration) investigated.

Three hydrate generation experiments have been conducted, under the subcooling $\Delta T \approx 2$ °C (with either SDS or AOT) and $\Delta T \approx 4$ °C (SDS only), the latter condition being that previously examined by Venet et al.[55] Videographs of the meniscus region where hydrate crystals are generated are available in the Supporting Information, labeled after the surfactant promoter, SDS or AOT, the subcooling $\Delta T \approx 2$ °C (2C) or 4 °C (4C), and frames per second (1 or 30 FPS). For instance, VSDS2C30FPS refers to a video of SDS-promoted

https://doi.org/10.1021/acsomega.4c03251
ACS Omega 2024, 9, 31842−31854

hydrate generated under a subcooling of 2 °C with 30 frames per second. High FPS (30 FPS) is used to capture a short time interval with high temporal resolution, here the crystal formation and growth on the meniscus in the early stages of the hydrate generation process. Low-FPS (1 FPS) videographs are used to extract the meniscus displacement and water conversion ratios τ_w (see equation 4) over the whole duration of step 3. These ratios are plotted in Figures 4 and 5 as

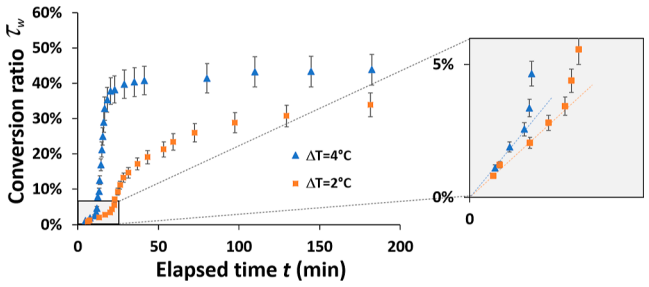

Figure 5. Conversion ratio or meniscus displacement—both quantities are proportional, see eq 4—as a function of time t for SDS-promoted hydrate at $\Delta T \approx 2$ °C and 4 °C.

functions of the time elapsed from the onset of hydrate generation. These two figures, respectively, compare the effects on hydrate growth of SDS and AOT (with concentrations 500 ppmw) under the same subcooling $\Delta T \approx 2$ °C and of two different temperatures or subcoolings ($\Delta T \approx 2$ and 4 °C) for the same surfactant (SDS). The porosities of the resulting porous hydrates and the hydration numbers are also determined and discussed at the end of this section (see Table 1).

Table 1. Porosity and Final Conversion Ratios of SDS- and AOT-Promoted Methane Hydrates as Obtained from Meniscus Displacements Δl_{wh} and Δl_{wg}

methane hydrate growth conditions	l_{w_0} (mm)	Δl_{wh} (mm)	Δl_{wg} (mm)	τ_{wf} (%)	ϕ (%)	N_h
$\Delta T \approx 2$ °C, 40 bar, SDS 500 ppmw	9.24	0.81	8.33*	34[a]	61[c]	5.9
				35[b]	60[d]	
$\Delta T \approx 2$ °C, 40 bar, AOT 500 ppmw	8.82	0.53	10.51	23[a]	72[c]	5.9
				24[b]	70[d]	
$\Delta T \approx 4$ °C, 40 bar, SDS 500 ppmw	10.36	1.17	18.62**	44[a]	50[c]	6.0
				44[b]	50[d]	

Calculated from a: eq 7, b: eq 12, c: eq 8, and d: eq 16. *Obtained by increasing P and T to P_d = 72.0 bar and T_d=10 °C. **Obtained by increasing P and T to P_d = 104 bar and T_d = 20 °C.

As presented and discussed in the next subsections, the hydrate generation and growth process obeys a complex behavior characterized by two different regimes: first, a relatively slow process, in which individual hydrate crystals are generated around the top (or apex) of the meniscus and expelled into the aqueous phase where they form a slurry; a few minutes later, the generation process accelerates drastically, with changes in the meniscus region (see below), and a fast conversion regime sets in. In the late stages, the meniscus advance (and hence the conversion rate) slows down as the slurry of hydrate crystals reaches the closed end of the capillary and becomes increasingly packed and compressed.

4.1.1. Early Steady-State Generation Regime. The presence of tiny amounts (here, 500 ppmw) of an anionic surfactant in the aqueous phase drastically changes the hydrate generation and growth process at water/gas interfaces. Supporting Information videos VSDS2C30FPS and VSDS4C30FPS as well as the early stages of VAOT2C1FPS show that, rather than forming a thin impermeable polycrystalline layer over these interfaces (as they are in the absence of a surfactant),[53,72] the hydrate crystals generated on the meniscus are hollow crystals growing into the water phase from their basis on the interfaces, a closed (triple) line where the hydrate phase is in contact with both the aqueous and gas phases, thus allowing the hydrate growth to proceed. They are irregular in shape (looking like spikes, cones, etc.) and expand quickly on the aqueous side of the interface, with their interior filled with the gas phase (methane) and their exterior surrounded by the aqueous phase (see also the snapshots extracted from these videographs at the bottom of Figure 4). They grow more slowly and to a larger extent and therefore are more easily distinguished at $\Delta T \approx 2$ °C than at $\Delta T \approx 4$ °C (compare videos VSDS2C30FPS and VSDS4C30FPS). Their dark appearance, similar to that of bulk gas, is the result of the incoming light being refracted (the gas has a low refractive index, close to 1) and hence not reaching the objective of the microscope. As long as their basis remains in contact with the meniscus, the hydrate crystals keep growing from their basis at high rates, in the range of a few μm/s at $\Delta T \approx 2$ °C and >10 μm/s at $\Delta T \approx 4$ °C, until reaching lengths up to a few tens of μm when they end up being abruptly invaded by water (they no longer refract light and thin hydrate walls are barely visible), possibly as a result of mechanical failure. These crystals are finally expelled into the water phase and add to the slurry of gas hydrates, leaving the water/gas interface available for the generation of new crystals.

In all three experiments, the meniscus is observed to move first at a constant and rather low rate: this defines the early steady-state regime (see the insets in Figures 4 and 5). Under a subcooling $\Delta T \approx 2$ °C, both SDS and AOT induce a similar conversion rate $d\tau_w/dt \approx 1.75 \times 10^{-3}$ mol/mol per minute, meaning that, every minute, 0.175% of the water initially present is converted into methane hydrate. This rather slow growth process lasts about 5 min in the case of AOT and 20 min in the case of SDS, corresponding, respectively, to only ≈0.9 and 3.4% of the water being converted into methane hydrate (see Figure 4). Then there is an abrupt transition to rapid growth, which is presented and discussed in the next subsection.

When subcooling, which is the driving force for hydrate generation and growth, is increased from 2 to 4 °C, the water conversion rate $d\tau_w/dt$ increases as expected, consistent with the observed more rapid generation of individual crystals on the meniscus, from 1.75×10^{-3} min^{-1} at $\Delta T \approx 2$ °C to 2.4×10^{-3} min^{-1} at $\Delta T \approx 4$ °C (see Figure 5). The transition to rapid growth (see the next subsection) occurs earlier at $\Delta T \approx 4$ °C than at $\Delta T \approx 2$ °C.

4.1.2. Rapid Conversion. The early steady-state growth transitions abruptly, within a few tens of seconds, to a regime of rapid conversion, in which the crystals generated on the meniscus become tinier, and the meniscus velocity and hence the conversion rate increases by about 1 order of magnitude. The conversion rate $d\tau_w/dt$ increases from 1.75×10^{-3} to 2.2×10^{-2} min^{-1} (AOT-promoted hydrate) and 1.3×10^{-2} min^{-1} (SDS-promoted hydrate) under a subcooling $\Delta T \approx 2$ °C and

https://doi.org/10.1021/acsomega.4c03251
ACS Omega 2024, 9, 31842−31854

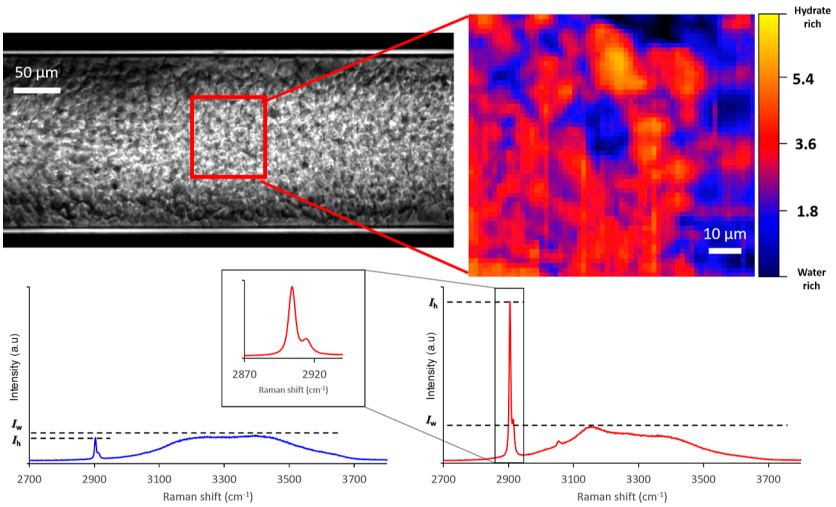

Figure 6. Snapshot obtained by transmission optical microscopy (upper left) and Raman (upper right) images of the porous AOT-promoted methane hydrate formed under a subcooling $\Delta T \approx 2$ °C at $P_{exp} = 40$ bar, featuring hydrate-rich (red) zones where $I_h > I_w$ and water-rich (blue) zones where $I_h < I_w$. I_w is the intensity of the O−H stretching modes of liquid water and I_h is the intensity of the C−H stretching modes of the enclathrated methane in the large and small cages of the structure I hydrate (see the pdf file in the Supporting Information).

from 2.4×10^{-3} to 6.8×10^{-2} min^{-1} under $\Delta T \approx 4$ °C (SDS-promoted hydrate), see Figures 4 and 5. Most of the overall water conversion into hydrate (from 24 to 44% in those experiments; see below) occurs in this regime, which lasts for a few minutes. The abrupt increase in the conversion rate is concomitant with two features that occur on/around the meniscus: (i) its flattening (with in some instances oscillations) with most of its surface (instead of only its top in the early steady-state regime) contributing to the generation of gas hydrates and (ii) a large amount of gas entering the slurry of hydrate crystals as a trail of dark dots that persists over a few hundreds of μm at the rear of the meniscus (see videos VSDS2C1FPS, VAOT2C1FPS and VSDS4C1FPS in the Supporting Information and the snapshots at the bottom of Figure 3). This trail of small-gas microdomains shrinks and eventually disappears as the microdomains move away from the meniscus. The large amount of water/gas interfacial area of those microdomains is likely responsible for the sudden increase observed in the conversion rate.

The transition from slow to rapid hydrate generation, as witnessed at a mesoscopic scale by the generation of hydrate crystals at the water/guest interface and at a macroscopic scale by the meniscus displacement (or water conversion), is observed to occur with both anionic surfactants, AOT and SDS, and with SDS for the two subcoolings investigated, $\Delta T \approx$ 2 and 4 °C. These observations are consistent with those by Zhang et al.[50] of methane hydrate promotion by SDS (with concentrations from 0.5 to 4 mmol/l, or from 144 to 1152 ppmw) at the water/methane interface, either in a thin glass capillary or in droplets of the SDS solution under pressurized methane in conditions close to ours. These authors report an aqueous phase/methane interface transitioning from an early regime of "slight fluctuations" to a regime of violent fluctuations or "boiling".[50]

While the hydrate generation and growth features appear to be qualitatively similar for the two anionic surfactants (and similar to those observed by other researchers),[50] there are quantitative differences: the transition to rapid hydrate generation occurs later with SDS than with AOT, which thus provides a quicker conversion into hydrate.

4.1.3. Late Stages: Completion of the Porous Hydrate. At later times, when the hydrate slurry reaches the closed end of the capillary (data not shown) and gets increasingly packed and compressed, the meniscus velocity indeed decreases and ultimately vanishes. A porous hydrate with a homogeneous and stable texture ends up filling the interval between the meniscus and the end of the capillary, with the *caveat* that the meniscus may experience some slight distortion and/or wall climbing in the very late stages.

Table 1 gathers the initial column lengths l_{w_0} and the meniscus displacements Δl_{wh} measured over the whole growth process and the corresponding final conversion ratios τ_{wf}, i.e., the asymptotic values of the conversion ratios at a large t, together with the porosities ϕ of the hydrate formed, as calculated by eqs 7 and 8. Δl_{wh} is a small fraction—typically 6−12%—of the initial column length l_{w_0}, and significant uncertainties are therefore attached to these values. As explained in the previous section, a more precise determination of τ_{wf} and ϕ is obtained from the displacements Δl_{wg} (also gathered in Table 1) induced by the released gas after melting the hydrate at the end of the experiment (eqs 12 and 16). As explained in the previous section, the latter displacement may however be so large that the capillary cannot be moved along its axis to the extent required to follow the meniscus position, and the gas volume (i.e., Δl_{wg}) is then reduced by increasing P to $P_d > P_{exp}$ while not causing hydrate reformation; a slight increase in T_d may also be required, see Table 1.

The overall conversion τ_{wf} and therefore porosities ϕ differ significantly for the two surfactant promoters and the two temperatures investigated. The porosity of AOT-promoted methane hydrate is larger ($\phi \approx 70\%$; $\tau_{wf} \approx 24\%$) than that of SDS-promoted methane hydrate (50−60%), which decreases with increasing subcooling, from ≈60% ($\tau_{wf} \approx 34\%$) for $\Delta T \approx$ 2 °C to ≈50% ($\tau_{wf} \approx 44\%$) for $\Delta T \approx 4$ °C. Each of the three experiments was replicated 2−3 times (only one set of data is shown here), and we observed variations in water conversions and porosities in the range of ±5%.

Clearly, SDS ensures a larger conversion of water into hydrate than AOT, which also increases with subcooling; equivalently, the SDS-promoted hydrate is less porous than the

https://doi.org/10.1021/acsomega.4c03251
ACS Omega 2024, 9, 31842−31854

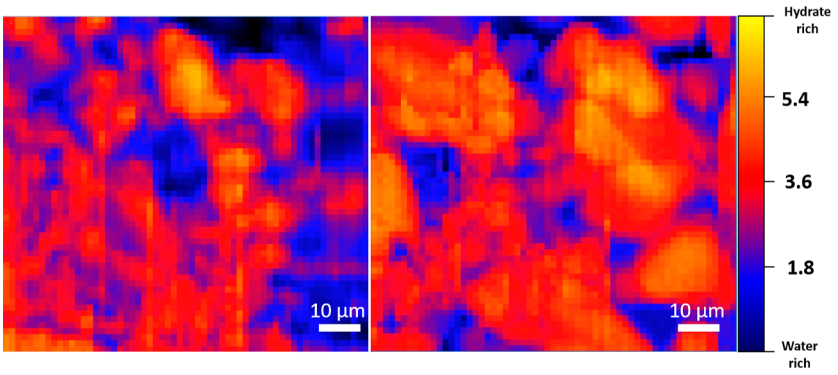

Figure 7. MicroRaman images (120 μm × 110 μm) of the AOT-promoted (left) and SDS-promoted (right) hydrate porous structures at 40 bar and $\Delta T \approx 2$ °C. The AOT-promoted hydrate is more porous and has larger pores than the SDS-promoted hydrate.

AOT-promoted one, and porosity decreases with increased subcooling. A more complete comparison and discussion of the two surfactant promoters and their respective efficiencies is presented in Section 5, once the porous structures of both hydrates have been characterized by microRaman spectroscopy (Section 4.2).

The hydration numbers N_h obtained from the measured displacements Δl_{wh} and Δl_{wg} and using eq 13 lie in the range 5.9−6.0 for the three experiments (rightmost column in Table 1), in agreement with the values—slightly larger than 6—determined by various methods for methane hydrate, including those determined by Raman spectroscopy (see the next section). It is important to note that the values of hydration number N_h are determined from two meniscus displacements, themselves obtained from the measurement of two different lengths, and one of these displacements, Δl_{wh}, is a small fraction of the initial column length l_{w_0}, as explained earlier.

4.2. MicroRaman Spectroscopy Mapping of the Porous Hydrate. A micro-Raman mapping of the porous hydrate is carried out at the end of step 3 for each one of the three experiments described in previous section. The procedure is the same as that by Venet et al.:[55] a ca. 0.1 × 0.1 mm^2 cross-section of the porous hydrate is selected and discretized into 2 × 2 μm^2 pixels, and the Raman spectra in the spectral window 2800−3800 cm^{-1} are acquired for each pixel, with the purpose of determining the predominance of either liquid water or methane hydrate. The Raman spectra exhibit a broad band associated with the symmetric and antisymmetric O−H stretching modes of liquid water in the interval 3000−3600 cm^{-1} and two pronounced peaks associated with the C−H stretching modes of methane in the large and small cages of the structure I hydrate (Raman shifts at 2903 and 2914 cm^{-1}, respectively).[2,65] The intensity or surface area of those two peaks are related to the filling of these cages with methane, cf. next subsection and the pdf file in the Supporting Information. The relative intensity I_h/I_w of the sharp hydrate peaks relative to that of the broad liquid water band provides an indication as to local composition: when this ratio is large, the hydrate is the prevailing phase, whereas liquid water is predominant when this ratio is small, cf. Figure 6.

Only the microRaman images of the AOT- and SDS-promoted methane hydrates prepared under a subcooling $\Delta T \approx 2$ °C (P = 40 bar) are presented here; see Figure 7. (The data for the SDS-promoted hydrate at $\Delta T \approx 4$ °C are not shown: some of them can be found in Venet et al.[55]) The average intensity ratios I_h/I_w are, respectively, equal to 2.0 and 2.8, showing that there is more liquid water (or porosity) in the AOT-promoted hydrate than in the SDS-promoted hydrate, consistent with the trends determined by mass balance (see previous subsection). A porosity value could, in principle, be obtained by a segmentation procedure in which a particular threshold for the ratio I_h/I_w is chosen that delineates pixels belonging to the hydrate skeleton from pixels belonging to the pore volume. Indeed, this value depends on the chosen threshold, which precludes the use of this procedure for quantitative estimates. However, it can be used for comparison purposes. Interestingly, we observe that, irrespective of the threshold chosen in a reasonable range, the differences between the porosities of the AOT-promoted and SDS-promoted hydrate structures lie in the 10% range, in line with the difference obtained by material balance (see Table 1).

These images also reveal the sizes of water- and hydrate-rich heterogeneities, which can be identified as the pores and grains of the porous hydrate. Pore sizes of the SDS-promoted hydrate are in the range of 10−20 μm, consistent with the value inferred from the rate of imbibition by liquid water of a similar porous hydrate.[55] They are somewhat larger in the AOT-promoted hydrate (Figure 7).

The area of Raman peaks associated with the stretching modes of methane in the large (2903 cm^{-1}) and small (2914 cm^{-1}) cages of the sI methane hydrate can be related to the absolute occupancies of the large (θ_{L_c}) and small (θ_{S_c}) cages by using the van der Waals Platteuw formalism described in the pdf file of the Supporting Information. The results for the AOT- and SDS-promoted methane hydrates are displayed in Table 2. The large cages are almost completely filled and the small cages are approximately 83−84% filled with methane, in agreement with the literature results for methane hydrates formed in the absence of additives under similar T and P conditions.[64−68,73−75] The results given in Table 2 for the filling of small cages are values averaged over Gaussian distributions, with a standard deviation of ≈4%. The hydration

Table 2. Cage Filling and Hydration Number as Determined by Means of MicroRaman Spectroscopy

methane hydrate growth conditions	θ_{S_c} (%)	θ_{L_c} (%)	N_h
$\Delta T \approx 2$ °C, 40 bar, SDS 500 ppmw	83	99	6.04
$\Delta T \approx 2$ °C, 40 bar, AOT 500 ppmw	84	99	6.03
$\Delta T \approx 4$ °C, 40 bar, SDS 500 ppmw	84	99	6.03

https://doi.org/10.1021/acsomega.4c03251
ACS Omega 2024, 9, 31842−31854

number inferred from the absolute cage occupancies is found to be very close to 6 (Table 2).

To the best of our knowledge, the absence of any effect of an anionic surfactant promoter on the hydrate cage filling has never been shown before. Sun et al.[64] recently measured the absolute cage occupancies of sI methane hydrates in the presence of a cationic surfactant, namely, cetyltrimethylammonium bromide. They did not either observe any significant effect of this surfactant on cage filling as well on the hydration number N_h.

5. DISCUSSION

A discussion of the respective efficiencies of the two methane hydrate promoters, SDS and AOT, is in order. As mentioned above, the mesoscopic and macroscopic features of hydrate generation at the water/guest interface are similar for both promoters, and the resulting porous hydrates have a similar texture, characterized by a high porosity in the 50−70% range and pore sizes in the tens of microns. The molecular properties of methane hydrates, namely, the structure and cage filling by methane of the hydrate, are not altered by the surfactant promoter. Yet, there are quantitative differences in i) the transition to rapid conversion, which occurs earlier with AOT than with SDS and ii) the overall or final conversion of water into hydrate, which is larger with SDS than with AOT.

In other words, SDS converts more water into hydrate than AOT does but requires more time to do so. Two types of promoter efficiencies are distinguished, which are of interest for different gas-hydrate-based applications. One efficiency is the rapid conversion into a gas hydrate of water and gas phases contacting each other: it is of interest for continuous flow processes, e.g., for gas separation applications. AOT, in this respect, is a better promoter than SDS. The other efficiency is the ability of the promoter to convert a large quantity of water or guest molecules available, irrespective of the time spent: it is of interest, e.g., for gas storage applications. SDS, in this respect, is a better promoter than AOT.

The more rapid water conversion or hydrate generation observed with AOT is a reflection of the earlier transition from the early (slow) hydrate generation regime to the rapid conversion regime. The physical reasons that drive the AOT-containing system to more quickly enter the rapid conversion regime are unclear. The abrupt transition to the rapid conversion regime seems to have analogies with the transition observed with liquid/vapor menisci undergoing evaporative cooling at a high enough thermal gradient. The transition, which involves Marangoni-type effects, is to an unstable interface that enhances heat and mass transfers.[76]

A high hydrate generation on the meniscus and a rapid motion of the slurry in the direction opposite to the meniscus go with a strong backflow of water to the meniscus, as the hydrate and liquid water are nearly incompressible. This arrival of water to the meniscus ensures the continuation of hydrate generation, which indeed slows down when the hydrate crystals can no longer be evacuated away from the meniscus, i.e., when the hydrate slurry reaches the closed end of the capillary and starts to be compressed and transformed into a porous medium. In addition, the pores of the AOT-promoted hydrate (and very likely those of the hydrate slurry) are larger than those of the SDS-promoted hydrate, allowing a more rapid water backflow inside the hydrate slurry.

6. SUMMARY AND PROSPECTS

A novel experimental methodology has been designed that involves thin glass capillaries used both as optical cells and microreactors for the simultaneous observation and quantification of the generation, growth kinetics, and porous structure of gas hydrates promoted by additives. This methodology, which has been implemented with two surfactant additives, SDS and AOT, known to be efficient gas hydrate promoters, could be applied to any other additive or a combination of additives. The combination of optical microscopy and microRaman spectroscopy imaging provides precise information, over a large range of scales, on promoter properties that are key for the development of gas-hydrate-based technologies: the water- or gas-to-hydrate conversion rate and the overall conversion or storage capacity of the hydrate formed.

Similar features are observed for the low-to-moderate subcooling and the two promoters investigated, which both induce an abrupt transition from a slow production of hollow crystals on the water/guest interface at early times to a rapid conversion process in which the hydrate crystals are steadily and rapidly expelled on the aqueous side of the interface. In a finite volume, conversion slows down when the growing slurry of hydrate crystals consolidates into a porous medium, whose porosity and pore sizes are quantitatively characterized. The methodology allows a quantitative assessment of the conversion kinetics and final conversion or, equivalently, the porosity of the hydrate, whose pore sizes are observed to lie in the 10−30 μm for the promoters and conditions considered. It also allows us to discriminate important features of the gas hydrate generation process, such as the onset of rapid conversion and the conversion rate, of interest for continuous flow processes (e.g., gas separation processes), and the final conversion ratio, of interest for gas storage. As an example, the final conversion is higher (i.e., hydrate porosity is lower) with SDS than with AOT, which, however, converts water and gas into gas hydrate more rapidly than SDS.

Additionally, microRaman spectroscopy provides molecular-scale information as to hydrate cage filling and hydration number, whose values are observed to be similar to those of additive-free methane hydrate for the two additives investigated, both having only a kinetic effect on hydrate formation.

A high conversion rate does not necessarily go hand in hand with a large final conversion ratio or water (or gas) uptake, and vice-versa. The physicochemical processes that control the onset to rapid conversion and the properties (pore size, porosity) of the resulting porous hydrate deserve to be better understood and necessitate further investigation. Future work should concentrate on testing other gas hydrate promoters or a combination of promoters as well as operational parameters (promoter concentration, subcooling) that, depending on the application, foster either rapid conversion or a high final conversion ratio (or, equivalently, a low final hydrate porosity). The proposed methodology could and should be applied to other guest molecules and thus provide a better understanding of the growth mechanisms and a determination of the optimal conditions for fast or high gas hydrate conversion.

■ ASSOCIATED CONTENT

Supporting Information

The following files are available: The Supporting Information is available free of charge at https://pubs.acs.org/doi/10.1021/acsomega.4c03251.

https://doi.org/10.1021/acsomega.4c03251
ACS Omega 2024, 9, 31842−31854

Supporting Information—Procedure to determine the meniscus positions and displacements, evaluation of associated errors, examples of Raman peaks of methane enclathrated in large and small cages of cubic sI methane hydrate, and definition and discussion of storage capacity and its relation to the metrics introduced in the study (PDF)

TCYCLE—Temperature cycle used in the experiment to trigger and study hydrate generation at a specified temperature and then dissociate the hydrate (MP4)

MATBAL—Illustrative video to explain the method used in this study that exploits the meniscus displacements to calculate the conversion rates of water into hydrate and the conversion ratio or porosity of the porous hydrate formed (MP4)

VAOT2C1FPS—AOT-promoted methane hydrate generation at the gas−liquid interface under a subcooling $\Delta T \approx 2$ °C, with the video recorded at 1 frame per second and sped up by a factor 14, showing two regimes—an early slow generation regime, followed by a rapid conversion regime (MP4)

VSDS2C1FPS—SDS-promoted methane hydrate generation at the gas−liquid interface under a subcooling $\Delta T \approx 2$ °C, with the video recorded at 1 frame per second and sped up by a factor 14, but not accelerated nor slowed, showing two regimes—an early slow generation regime, followed by rapid conversion (MP4)

VSDS4C1FPS—SDS-promoted methane hydrate generation at the gas−liquid interface under a subcooling $\Delta T \approx 4$ °C, with the video recorded at 1 frame per second and sped up by a factor 14, showing two regimes—an early slow generation regime, followed by rapid conversion (MP4)

VSDS2C30FPS—SDS-promoted methane hydrate generation at the gas−liquid interface under a subcooling $\Delta T \approx 2$ °C, with the video recorded at 30 frames per second neither sped up nor slowed down, showing only the early slow generation regime (MP4)

VSDS4C30FPS—SDS-promoted methane hydrate generation at the gas−liquid interface under a subcooling $\Delta T \approx 4$ °C, with the video recorded at 30 frames per second neither sped up nor slowed down, showing only the early slow generation regime (MP4)

AUTHOR INFORMATION

Corresponding Authors

Belkacem Samar − *Université de Pau et des Pays de l'Adour, E2S UPPA, CNRS, LFCR, Pau 64013, France;* orcid.org/0000-0002-0963-008X; Email: bsamar@univ-pau.fr

Daniel Broseta − *Université de Pau et des Pays de l'Adour, E2S UPPA, CNRS, LFCR, Pau 64013, France;* orcid.org/0000-0001-9346-4370; Email: daniel.broseta@univ-pau.fr

Authors

Saphir Venet − *Université de Pau et des Pays de l'Adour, E2S UPPA, CNRS, LFCR, Pau 64013, France;* orcid.org/0009-0001-3224-921X

Arnaud Desmedt − *Université de Bordeaux, ISM UMR5255 CNRS, Talence Cedex 33405, France; Laboratoire Léon Brillouin, UMR12 CEA-CNRS, Gif-sur-Yvette 91190, France;* orcid.org/0000-0002-4737-7732

Complete contact information is available at: https://pubs.acs.org/10.1021/acsomega.4c03251

Notes

The authors declare no competing financial interest.

ACKNOWLEDGMENTS

The authors thank the French National Research Agency (ANR) for partly funding the present study via the France 2030 investment plan. This work is part of the project PEPR ANR-22-PESP-0007. The authors also thank the researchers of The Molecular Spectroscopy Group of the Institute of Molecular Sciences for their expertise and help. This research was also supported by CNRS Groupement De Recherche (GDR) "Hydrates de Gaz".

REFERENCES

(1) Sloan, E. D.; Koh, C. A. *Clathrate Hydrates of Natural Gases*; CRC Press, 2007.

(2) Ripmeester, J. A.; Alavi, S. *Clathrate Hydrates, 2 Volumes: Molecular Science and Characterization*; John Wiley & Sons, 2022.

(3) Linga, P.; Kumar, R.; Lee, J. D.; Ripmeester, J.; Englezos, P. A new apparatus to enhance the rate of gas hydrate formation: Application to capture of carbon dioxide. *Int. J. Greenh. Gas Control* **2010**, *4*, 630−637.

(4) Kumar, A.; Bhattacharjee, G.; Kulkarni, B. D.; Kumar, R. Role of Surfactants in Promoting Gas Hydrate Formation. *Ind. Eng. Chem. Res.* **2015**, *54*, 12217−12232.

(5) He, Y.; Sun, M.-T.; Chen, C.; Zhang, G.-D.; Chao, K.; Lin, Y.; Wang, F. Surfactant-based promotion to gas hydrate formation for energy storage. *J. Mater. Chem. A* **2019**, *7*, 21634−21661.

(6) Hassanpouryouzband, A.; Joonaki, E.; Vasheghani Farahani, M.; Takeya, S.; Ruppel, C.; Yang, J.; English, N. J.; Schicks, J. M.; Edlmann, K.; Mehrabian, H.; et al. Gas hydrates in sustainable chemistry. *Chem. Soc. Rev.* **2020**, *49*, 5225−5309.

(7) Englezos, P. Technology readiness level of gas hydrate technologies. *Can. J. Chem. Eng.* **2023**, *101*, 3034−3043.

(8) Veluswamy, H. P.; Kumar, A.; Seo, Y.; Lee, J. D.; Linga, P. A review of solidified natural gas (SNG) technology for gas storage via clathrate hydrates. *Appl. Energy* **2018**, *216*, 262−285.

(9) Yin, Z.; Zheng, J.; Kim, H.; Seo, Y.; Linga, P. Hydrates for cold energy storage and transport: A review. *Adv. Appl. Energy* **2021**, *2*, 100022.

(10) Ma, Z.; Zhang, P.; Bao, H.; Deng, S. Review of fundamental properties of CO2 hydrates and CO2 capture and separation using hydration method. *Renew. Sustain. Energy Rev.* **2016**, *53*, 1273−1302.

(11) Broseta, D.; Dicharry, C.; Torré, J.-P. Hydrate-Based Removal of CO2 from CH4+ CO2 Gas Streams. In *Gas Hydrates 2: Geoscience Issues and Potential Industrial Application*; Wiley, 2018; pp 285−314.

(12) Wu, L.-M.; Li, X.-Y.; Xie, F.-M.; Zhong, D.-L.; Englezos, P.; Yan, J. Minireview of Hydrate-Based CO2 Separation from a CO2/CH4 Gas Mixture: Progress and Outlook. *Energy Fuels* **2022**, *36*, 10478−10488.

(13) Di Profio, P.; Ciulla, M.; Di Giacomo, S.; Barbacane, N.; Wolicki, R. D.; Fontana, A.; Moffa, S.; Pilato, S.; Siani, G. Emerging green strategies for biogas upgrading through CO2 capture: From unconventional organic solvents to clathrate and semi-clathrate hydrates. *J. Mol. Liq.* **2023**, *391*, 123196.

(14) Simmons, B. A.; Bradshaw, R. W.; Dedrick, D. E.; Cygan, R. T.; Greathouse, J. A.; Majzoub, E. H. *Desalination Utilizing Clathrate Hydrates (LDRD Final Report)*; Sandia National Laboratories, 2008.

(15) Babu, P.; Nambiar, A.; He, T.; Karimi, I. A.; Lee, J. D.; Englezos, P.; Linga, P. A review of clathrate hydrate based desalination to strengthen energy−water nexus. *ACS Sustain. Chem. Eng.* **2018**, *6*, 8093−8107.

(16) Li, G.; Hwang, Y.; Radermacher, R. Review of cold storage materials for air conditioning application. *Int. J. Refrig.* **2012**, *35*, 2053−2077.
(17) Delahaye, A.; Fournaison, L.; Dalmazzone, D. Use of Hydrates for Cold Storage and Distribution in Refrigeration and Air-Conditioning Applications. In *Gas Hydrates 2: Geoscience Issues and Potential Industrial Applications*; Wiley, 2018; pp 315−358.
(18) Wang, X.; Zhang, F.; Lipiński, W. Carbon dioxide hydrates for cold thermal energy storage: A review. *Sol. Energy* **2020**, *211*, 11−30.
(19) Kalogerakis, N.; Jamaluddin, A.; Dholabhai, P.; Bishnoi, P. Effect of surfactants on hydrate formation kinetics. In *SPE International Symposium on Oilfield Chemistry*; Onepetro, 1993.
(20) Ganji, H.; Manteghian, M.; Sadaghiani zadeh, K.; Omidkhah, M.; Rahimi Mofrad, H. Effect of different surfactants on methane hydrate formation rate, stability and storage capacity. *Fuel* **2007**, *86*, 434−441.
(21) Ricaurte, M.; Dicharry, C.; Broseta, D.; Renaud, X.; Torré, J. P. CO2 Removal from a CO2−CH4 Gas Mixture by Clathrate Hydrate Formation Using THF and SDS as Water-Soluble Hydrate Promoters. *Ind. Eng. Chem. Res.* **2013**, *52*, 899−910.
(22) Bamaga, O.; Ahmed, I.; Wafiyah, A. M.; Albeirutty, M.; Abulkhair, H.; Shaiban, A.; Linga, P. Studies on Methane Gas Hydrate Formation Kinetics Enhanced by Isopentane and Sodium Dodecyl Sulfate Promoters for Seawater Desalination. *Energies* **2022**, *15*, 9652.
(23) Perrin, A.; Celzard, A.; Marêché, J. F.; Furdin, G. Methane Storage within Dry and Wet Active Carbons: A Comparative Study. *Energy Fuels* **2003**, *17*, 1283−1291.
(24) Celzard, A.; Marêché, J. Optimal wetting of active carbons for methane hydrate formation. *Fuel* **2006**, *85*, 957−966.
(25) Wu, Y.; Tang, T.; Shi, L.; He, Y. Rapid hydrate-based methane storage promoted by bilayer surfactant-coated Fe3O4 nanoparticles under a magnetic field. *Fuel* **2021**, *303*, 121248.
(26) Deng, Z.; Wang, Y.; Yu, C.; Li, G.; Lang, X.; Wang, S.; Fan, S. Promoting methane hydrate formation with expanded graphite additives: Application to solidified natural gas storage. *Fuel* **2021**, *299*, 120867.
(27) Mahant, B.; Patel, D.; Kushwaha, O. S.; Kumar, R. Systematic Study of Nanohybrids of ZnO Nanoparticles toward Enhancement of Gas Hydrate Kinetics and the Application in Energy Storage. *Energy Fuels* **2023**, *37*, 19621−19638.
(28) Omran, A.; Nesterenko, N.; Valtchev, V. Driving sustainable energy storage: A multi-scale investigation of methane hydrate formation with green promoters and innovative reactor design. *J. Energy Storage* **2024**, *75*, 109653.
(29) Ndlovu, P.; Babaee, S.; Naidoo, P.; Moodley, K. Utilization of Nanoparticles to Improve the Kinetics of CH4 Gas Hydrates in Gas Storage Applications. *Energy Fuels* **2024**, *38*, 4480−4491.
(30) Mu, L.; Zhao, H.; Zhou, Z.; Zeng, J.; Cui, Q. Improving Methane Hydrate Formation Kinetics and Gas Storage Capacity with a Promoter. *Energy Fuels* **2023**, *37*, 14778−14789.
(31) Kutergin, O.; Melnikov, B.; Nesterov, A. Influence of Surfactants on the Mechanism and Kinetics of Gas Hydrate Formation. *Doklady Akademii Nauk SSSR*, 1992; Vol. *323*, pp 549−553.
(32) Mel'nikov, V.; Nesterov, A.; Feklistov, V. Formation of gas hydrates in the presence of additives consisting of surface-active substances. *Khimiya V. Interes. Ustoychivogo Razvit.* **1998**, *6*, 97−102.
(33) Zhong, Y.; Rogers, R. Surfactant effects on gas hydrate formation. *Chem. Eng. Sci.* **2000**, *55*, 4175−4187.
(34) Link, D. D.; Ladner, E. P.; Elsen, H. A.; Taylor, C. E. Formation and dissociation studies for optimizing the uptake of methane by methane hydrates. *Fluid Phase Equilib.* **2003**, *211*, 1−10.
(35) Gayet, P.; Dicharry, C.; Marion, G.; Graciaa, A.; Lachaise, J.; Nesterov, A. Experimental determination of methane hydrate dissociation curve up to 55 MPa by using a small amount of surfactant as hydrate promoter. *Chem. Eng. Sci.* **2005**, *60*, 5751−5758.
(36) Zhang, J.; Lee, S.; Lee, J. W. Kinetics of methane hydrate formation from SDS solution. *Ind. Eng. Chem. Res.* **2007**, *46*, 6353−6359.
(37) Botimer, J. D.; Dunn-Rankin, D.; Taborek, P. Evidence for immobile transitional state of water in methane clathrate hydrates grown from surfactant solutions. *Chem. Eng. Sci.* **2016**, *142*, 89−96.
(38) Di Profio, P.; Arca, S.; Germani, R.; Savelli, G. Surfactant promoting effects on clathrate hydrate formation: Are micelles really involved? *Chem. Eng. Sci.* **2005**, *60*, 4141−4145.
(39) Watanabe, K.; Niwa, S.; Mori, Y. H. Surface tensions of aqueous solutions of sodium alkyl sulfates in contact with methane under hydrate-forming conditions. *J. Chem. Eng. Data* **2005**, *50*, 1672−1676.
(40) Zhang, J.; Lee, S.; Lee, J. W. Solubility of sodium dodecyl sulfate near propane and carbon dioxide hydrate-forming conditions. *J. Chem. Eng. Data* **2007**, *52*, 2480−2483.
(41) Zhang, J.; Lee, S.; Lee, J. W. Does SDS micellize under methane hydrate-forming conditions below the normal Krafft point? *J. Colloid Interface Sci.* **2007**, *315*, 313−318.
(42) Ando, N.; Kuwabara, Y.; Mori, Y. H. Surfactant effects on hydrate formation in an unstirred gas/liquid system: An experimental study using methane and micelle-forming surfactants. *Chem. Eng. Sci.* **2012**, *73*, 79−85.
(43) Sun, C.-Y.; Chen, G.-J.; Yang, L.-Y. Interfacial tension of methane+ water with surfactant near the hydrate formation conditions. *J. Chem. Eng. Data* **2004**, *49*, 1023−1025.
(44) Zhang, J.; Lo, C.; Somasundaran, P.; Lu, S.; Couzis, A.; Lee, J. W. Adsorption of sodium dodecyl sulfate at THF hydrate/liquid interface. *J. Phys. Chem. C* **2008**, *112*, 12381−12385.
(45) Lo, C.; Zhang, J.; Somasundaran, P.; Lu, S.; Couzis, A.; Lee, J. Adsorption of surfactants on two different hydrates. *Langmuir* **2008**, *24*, 12723−12726.
(46) Rauh, F.; Pfeiffer, J.; Mizaikoff, B. Infrared spectroscopy on the role of surfactants during methane hydrate formation. *RSC Adv.* **2017**, *7*, 39109−39117.
(47) Verrett, J.; Posteraro, D.; Servio, P. Surfactant effects on methane solubility and mole fraction during hydrate growth. *Chem. Eng. Sci.* **2012**, *84*, 80−84.
(48) Wang, F.; Wang, L.; Wang, C.; Guo, G.; Liu, G.; Luo, S.; Guo, R. Direction controlled methane hydrate growth. *Cryst. Growth Des.* **2015**, *15*, 5112−5117.
(49) Liu, Z.; Li, Y.; Wang, W.; Song, G.; Lu, Z.; Ning, Y.; Liu, S. Experimental investigation on the micro-morphologies and growing process of methane hydrate formation in SDS solution. *Fuel* **2021**, *293*, 120320.
(50) Zhang, X.; Zhao, J.; Chen, C.; Yuan, H.; Zhang, Y.; He, Y.; Wang, F. SDS-promoted methane hydrate growth in presence of a superhydrophobic substrate. *Chem. Eng. Sci.* **2023**, *276*, 118761.
(51) Sun, C.-Y.; Chen, G.-J.; Ma, C.-F.; Huang, Q.; Luo, H.; Li, Q.-P. The growth kinetics of hydrate film on the surface of gas bubble suspended in water or aqueous surfactant solution. *J. Cryst. Growth* **2007**, *306*, 491−499.
(52) Lee, S. Y.; Kim, H. C.; Lee, J. D. Morphology study of methane−propane clathrate hydrates on the bubble surface in the presence of SDS or PVCap. *J. Cryst. Growth* **2014**, *402*, 249−259.
(53) Daniel-David, D.; Guerton, F.; Dicharry, C.; Torré, J. P.; Broseta, D. Hydrate growth at the interface between water and pure or mixed CO2/CH4 gases: Influence of pressure, temperature, gas composition and water-soluble surfactants. *Chem. Eng. Sci.* **2015**, *132*, 118−127.
(54) Hayama, H.; Mitarai, M.; Mori, H.; Verrett, J.; Servio, P.; Ohmura, R. Surfactant effects on crystal growth dynamics and crystal morphology of methane hydrate formed at gas/liquid interface. *Cryst. Growth Des.* **2016**, *16*, 6084−6088.
(55) Venet, S.; Guerton, F.; Desmedt, A.; Broseta, D. Insights into the porous structure of surfactant-promoted gas hydrate. *Chem. Eng. Sci.* **2022**, *248*, 117193.
(56) Touil, A.; Broseta, D.; Desmedt, A. Gas hydrate crystallization in thin glass capillaries: Roles of supercooling and wettability. *Langmuir* **2019**, *35*, 12569−12581.

https://doi.org/10.1021/acsomega.4c03251
ACS Omega 2024, 9, 31842−31854

(57) Atig, D.; Broseta, D.; Pereira, J.-M.; Brown, R. Contactless probing of polycrystalline methane hydrate at pore scale suggests weaker tensile properties than thought. *Nat. Commun.* **2020**, *11*, 3379.
(58) Wang, F.; Liu, C.; Lu, W.; Wang, J.; Ye, Y. In situ Raman spectroscopic observation of the temperature-dependent partition of CH4 and CO2 during the growth of double hydrate from aqueous solution. *Can. J. Chem.* **2015**, *93*, 970−975.
(59) Ou, W.; Lu, W.; Qu, K.; Geng, L.; Chou, I.-M. In situ Raman spectroscopic investigation of flux-controlled crystal growth under high pressure: A case study of carbon dioxide hydrate growth in aqueous solution. *Int. J. Heat Mass Transfer* **2016**, *101*, 834−843.
(60) Sun, J.; Xin, Y.; Chou, I.-M.; Sun, R.; Jiang, L. Hydrate stability in the H2S−H2O system-visual observations and measurements in a high-pressure optical cell and thermodynamic models. *J. Chem. Eng. Data* **2020**, *65*, 3884−3892.
(61) Sun, J.; Chou, I.-M.; Jiang, L.; Lin, J.; Sun, R. Crystallization behavior of the hydrogen sulfide hydrate formed in microcapillaries. *ACS Omega* **2021**, *6*, 14288−14297.
(62) Li, Y.; Gambelli, A. M.; Rossi, F.; Mei, S. Effect of promoters on CO2 hydrate formation: Thermodynamic assessment and microscale Raman spectroscopy/hydrate crystal morphology characterization analysis. *Fluid Phase Equilib.* **2021**, *550*, 113218.
(63) Li, Y.; Maria Gambelli, A.; Chen, J.; Yin, Z.; Rossi, F.; Tronconi, E.; Mei, S. Experimental study on the competition between carbon dioxide hydrate and ice below the freezing point. *Chem. Eng. Sci.* **2023**, *268*, 118426.
(64) Sun, J.; Jiang, L.; Chou, I. M.; Nguyen, N. N.; Nguyen, A. V.; Chen, Y.; Lin, J.; Wu, C. Thermodynamic and kinetic study of methane hydrate formation in surfactant solutions: From macroscale to microscale. *Energy* **2023**, *282*, 128356.
(65) Sum, A. K.; Burruss, R. C.; Sloan, E. D. Measurement of clathrate hydrates via Raman spectroscopy. *J. Phys. Chem. B* **1997**, *101*, 7371−7377.
(66) Uchida, T.; Hirano, T.; Ebinuma, T.; Narita, H.; Gohara, K.; Mae, S.; Matsumoto, R. Raman spectroscopic determination of hydration number of methane hydrates. *AIChE J.* **1999**, *45*, 2641−2645.
(67) Chou, I.-M.; Sharma, A.; Burruss, R. C.; Shu, J.; Mao, H.-k.; Hemley, R. J.; Goncharov, A. F.; Stern, L. A.; Kirby, S. H. Transformations in methane hydrates. *Proc. Natl. Acad. Sci. U.S.A.* **2000**, *97*, 13484−13487.
(68) Qin, J.; Kuhs, W. F. Quantitative analysis of gas hydrates using Raman spectroscopy. *AIChE J.* **2013**, *59*, 2155−2167.
(69) Chazallon, B.; Noble, J. A.; Desmedt, A. Spectroscopy of gas hydrates: from fundamental aspects to chemical engineering, geophysical and astrophysical applications. In *Gas Hydrates 1: Fundamentals, Characterization and Modeling*; Wiley, 2017; pp 63−112.
(70) Handa, Y. P. Effect of hydrostatic pressure and salinity on the stability of gas hydrates. *J. Phys. Chem.* **1990**, *94*, 2652−2657.
(71) Lemmon, E. W.; Huber, M. L.; McLinden, M. O. *NIST Standard Reference Database 23: Reference Fluid Thermodynamic and Transport Properties-REFPROP*, version 8.0; NIST, 2007.
(72) Taylor, C. J.; Miller, K. T.; Koh, C. A.; Sloan, E. D. Macroscopic investigation of hydrate film growth at the hydrocarbon/water interface. *Chem. Eng. Sci.* **2007**, *62*, 6524−6533.
(73) Uchida, T.; Takeya, S.; Wilson, L.; Tulk, C.; Ripmeester, J.; Nagao, J.; Ebinuma, T.; Narita, H. Measurements of physical properties of gas hydrates and in situ observations of formation and decomposition processes via Raman spectroscopy and X-ray diffraction. *Can. J. Phys.* **2003**, *81*, 351−357.
(74) Qin, J.; Hartmann, C. D.; Kuhs, W. F. Cage occupancies of methane hydrates: Results from synchrotron X-ray diffraction and Raman spectroscopy. *arXiv* **2018**, arXiv:1803.02244.
(75) Constant Agnissan, A.; Guimpier, C.; Terzariol, M.; Fandino, O.; Chéron, S.; Riboulot, V.; Desmedt, A.; Ruffine, L. Influence of Clay-Containing Sediments on Methane Hydrate Formation: Impacts on Kinetic Behavior and Gas Storage Capacity. *J. Geophys. Res.: Solid Earth* **2023**, *128*, No. e2023JB027333.
(76) Sáenz, P. J.; Valluri, P.; Sefiane, K.; Karapetsas, G.; Matar, O. K. On phase change in Marangoni-driven flows and its effects on the hydrothermal-wave instabilities. *Phys. Fluids* **2014**, *26*, 024114.

https://doi.org/10.1021/acsomega.4c03251
ACS Omega 2024, 9, 31842−31854